

## MIT Open Access Articles

*Centrality dependence of proton and antiproton spectra in Pb+Pb collisions at 40A GeV and 158A GeV measured at the CERN Super Proton Synchrotron*

The MIT Faculty has made this article openly available. **Please share** how this access benefits you. Your story matters.

**Citation:** Anticic, T. et al. "Centrality dependence of proton and antiproton spectra in Pb+Pb collisions at 40A GeV and 158A GeV measured at the CERN Super Proton Synchrotron." Physical Review C 83.1 (2011) : n. pag. © 2011 The American Physical Society

**As Published:** <http://dx.doi.org/10.1103/PhysRevC.83.014901>

**Publisher:** American Physical Society

**Persistent URL:** <http://hdl.handle.net/1721.1/62863>

**Version:** Final published version: final published article, as it appeared in a journal, conference proceedings, or other formally published context

**Terms of Use:** Article is made available in accordance with the publisher's policy and may be subject to US copyright law. Please refer to the publisher's site for terms of use.



# Centrality dependence of proton and antiproton spectra in Pb + Pb collisions at 40A GeV and 158A GeV measured at the CERN Super Proton Synchrotron

T. Anticic,<sup>1</sup> B. Baatar,<sup>2</sup> D. Barna,<sup>3</sup> J. Bartke,<sup>4</sup> H. Beck,<sup>5</sup> L. Betev,<sup>6</sup> H. Białkowska,<sup>7</sup> C. Blume,<sup>5</sup> M. Bogusz,<sup>8</sup> B. Boimska,<sup>7</sup> J. Book,<sup>5</sup> M. Botje,<sup>9</sup> P. Bunčić,<sup>6</sup> T. Cetner,<sup>8</sup> P. Christakoglou,<sup>9</sup> P. Chung,<sup>10</sup> O. Chvala,<sup>11</sup> J. G. Cramer,<sup>12</sup> V. Eckardt,<sup>13</sup> Z. Fodor,<sup>3</sup> P. Foka,<sup>14</sup> V. Friese,<sup>14</sup> M. Gaździcki,<sup>5,15</sup> K. Grebieszko,<sup>8</sup> C. Höhne,<sup>14,\*</sup> K. Kadija,<sup>1</sup> A. Karev,<sup>6</sup> V. I. Kolesnikov,<sup>2</sup> M. Kowalski,<sup>4</sup> D. Kresan,<sup>14,\*</sup> A. Laszlo,<sup>3</sup> R. Lacey,<sup>10</sup> M. van Leeuwen,<sup>9</sup> M. Mackowiak,<sup>8</sup> M. Makariev,<sup>16</sup> A. I. Malakhov,<sup>2</sup> M. Mateev,<sup>17</sup> G. L. Melkumov,<sup>2</sup> M. Mitrovski,<sup>5</sup> S. Mrówczyński,<sup>15</sup> V. Nicolic,<sup>1</sup> G. Pál, A. D. Panagiotou,<sup>18</sup> W. Peryt,<sup>8</sup> J. Pluta,<sup>8</sup> D. Prindle,<sup>12</sup> F. Pühlhofer,<sup>19</sup> R. Renfordt,<sup>5</sup> C. Roland,<sup>20</sup> G. Roland,<sup>20</sup> M. Rybczyński,<sup>15</sup> A. Rybicki,<sup>4</sup> A. Sandoval,<sup>14</sup> N. Schmitz,<sup>13</sup> T. Schuster,<sup>5</sup> P. Seyboth,<sup>13</sup> F. Siklér,<sup>3</sup> E. Skrzypczak,<sup>21</sup> M. Slodkowski,<sup>8</sup> G. Stefanek,<sup>15</sup> R. Stock,<sup>5</sup> H. Ströbele,<sup>5</sup> T. Susa,<sup>1</sup> M. Szuba,<sup>8</sup> M. Utvić,<sup>5</sup> D. Varga,<sup>3,6</sup> M. Vassiliou,<sup>18</sup> G. I. Veres,<sup>3,20</sup> G. Vesztegombi,<sup>3</sup> D. Vranić,<sup>14</sup> Z. Włodarczyk,<sup>15</sup> and A. Wojtaszek-Szwarc<sup>15</sup>

(NA49 Collaboration)

<sup>1</sup>Rudjer Boskovic Institute, Zagreb, Croatia

<sup>2</sup>Joint Institute for Nuclear Research, Dubna, Russia

<sup>3</sup>KFKI Research Institute for Particle and Nuclear Physics, Budapest, Hungary

<sup>4</sup>Henryk Niewodniczanski Institute of Nuclear Physics, Polish Academy of Sciences, Cracow, Poland

<sup>5</sup>Fachbereich Physik der Universität, Frankfurt, Germany

<sup>6</sup>CERN, Geneva, Switzerland

<sup>7</sup>Institute for Nuclear Studies, Warsaw, Poland

<sup>8</sup>Faculty of Physics, Warsaw University of Technology, Warsaw, Poland

<sup>9</sup>National Institute for Nuclear Physics and High Energy Physics (NIKHEF), Amsterdam, The Netherlands

<sup>10</sup>Department of Chemistry, Stony Brook University (SUNYSB), Stony Brook, New York 11794, USA

<sup>11</sup>Charles University, Faculty of Mathematics and Physics, Institute of Particle and Nuclear Physics, Prague, Czech Republic

<sup>12</sup>Nuclear Physics Laboratory, University of Washington, Seattle, Washington 98195, USA

<sup>13</sup>Max-Planck-Institut für Physik, Munich, Germany

<sup>14</sup>Gesellschaft für Schwerionenforschung (GSI), Darmstadt, Germany

<sup>15</sup>Institute of Physics, Jan Kochanowski University, Kielce, Poland

<sup>16</sup>Institute for Nuclear Research and Nuclear Energy, Sofia, Bulgaria

<sup>17</sup>Atomic Physics Department, Sofia University St. Kliment Ohridski, Sofia, Bulgaria

<sup>18</sup>Department of Physics, University of Athens, Athens, Greece

<sup>19</sup>Fachbereich Physik der Universität, Marburg, Germany

<sup>20</sup>Massachusetts Institute of Technology (MIT), Cambridge, Massachusetts 02139, USA

<sup>21</sup>Institute for Experimental Physics, University of Warsaw, Warsaw, Poland

(Received 10 September 2010; revised manuscript received 7 December 2010; published 3 January 2011)

The yields of (anti)protons were measured by the NA49 Collaboration in centrality-selected Pb + Pb collisions at 40A and 158A GeV. Particle identification was obtained in the laboratory momentum range from 5 to 63 GeV/c by measuring the energy loss  $dE/dx$  in the time projection chamber detector gas. The corresponding rapidity coverage extends 1.6 units from midrapidity into the forward hemisphere. Transverse-mass spectra, the rapidity dependences of the average transverse mass, and rapidity density distributions were studied as a function of collision centrality. The values of the average transverse mass as well as the midrapidity yields of protons normalized to the number of wounded nucleons show only modest centrality dependences. In contrast, the shape of the rapidity distribution changes significantly with collision centrality, especially at 40A GeV. The experimental results are compared to calculations of the hadron-string dynamics and the ultrarelativistic quantum-molecular-dynamics transport models.

DOI: [10.1103/PhysRevC.83.014901](https://doi.org/10.1103/PhysRevC.83.014901)

PACS number(s): 25.75.Dw, 25.75.Ag

## I. INTRODUCTION

It is generally accepted that heavy-ion collisions at ultrarelativistic energies result in a fireball of matter with high density and temperature. Such conditions prevail when

the incoming nucleons deposit a sufficient amount of their kinetic energy in the reaction zone. Little is known about this stopping process and its relation to the stopping of the incident nucleons in elementary nucleon-nucleon interactions. There are three experimental approaches to study this question. In proton-nucleus ( $p + A$ ) collisions the difference between the center-of-mass (c.m.) energies of the incident and the most forward-going nucleon is a good measure of the stopped energy. This type of analysis has been pioneered in Ref. [1].

\*Present address: Fachbereich Physik der Universität Giessen, Germany.

Another approach to study effects owing to multiple projectile nucleon collisions employs symmetric collisions of nuclei of different size. The resulting distributions of participating nucleons in terms of longitudinal and transverse momenta may vary with the size of the incident nuclei. Such differences reflect the change of stopping power as a function of system size. Finally, the effective system size can be changed by varying the impact parameter in collisions between heavy nuclei. Here again the momentum distribution of participating nucleons may be different in central and peripheral collisions as a consequence of changes in the stopping behavior.

Energy loss in central collisions was studied as a function of beam energy at the alternating gradient synchrotron (AGS) in Brookhaven [2], at the CERN super proton synchrotron (SPS) in Geneva, [3] and at the relativistic heavy-ion collider (RHIC) in Brookhaven [4,5]. It was found that the proton rapidity distribution changes from a convex to a concave form from AGS to RHIC via SPS energies. At AGS energies the energy loss was also studied as a function of collision centrality [2]. A strong centrality dependence was observed. This topic has also been addressed by NA49 in two previous publications. The first one presents the net-proton distribution for central Pb + Pb collisions at 158A GeV [3]. The second one describes the measurement of midrapidity proton and antiproton yields in Pb + Pb collisions at various energies from 20A to 158A GeV as well as for different centralities at 158A GeV [6]. At RHIC the PHOBOS collaboration has published the centrality dependence of the rapidity density at midrapidity and the transverse-mass spectra of net protons [7] at  $\sqrt{s_{NN}} = 62.4$  GeV and charged particle pseudorapidity distributions [8,9] at  $\sqrt{s_{NN}} = 19.6, 62.4$ , and 130 GeV. Data on centrality-dependent particle production at  $y = 0$  and 1 in Au + Au collisions at  $\sqrt{s_{NN}} = 200$  GeV [10] are available from the BRAHMS collaboration. The STAR collaboration has published Au + Au data on the centrality dependence of proton and antiproton production at  $\sqrt{s_{NN}} = 130$  GeV [11] as well as at 62.4, 130, and 200 GeV [12]. Baryon transport is quantified by the ratio of net baryons near midrapidity to the number of participant nucleons.

In this paper we present the centrality dependence of proton and antiproton transverse mass and rapidity distributions in Pb + Pb collisions at 40A and 158A GeV as obtained with the NA49 detector [13]. The phase-space coverage extends in c.m. rapidity  $y$  from midrapidity 1.6 units into the forward hemisphere and ranges from zero to 2.0 GeV/c in transverse momentum  $p_T$ . Net-proton distributions at 158A GeV are obtained from those of all protons by subtracting the distributions of antiprotons. This analysis supplements the NA49 data on  $\pi$ ,  $K$ ,  $\phi$ , and  $\Lambda$  production as a function of beam energy at the CERN SPS [14–16].

## II. EXPERIMENTAL SETUP AND DATA SETS

The NA49 detector is a large acceptance hadron spectrometer at the CERN SPS [17]. The main components are four large time projection chambers (TPCs) and two superconducting dipole magnets with a 1-m vertical gap, aligned in a row, and a total bending power of 9 T m. Two 2-m-long TPCs [vertex TPCs (VTPCs)] inside the magnets, each with 72 pad rows along the beam direction, allow for precise tracking,

momentum determination, vertex reconstruction, and particle identification (PID) by the measurement of the energy loss ( $dE/dx$ ) in the detector gas. The other two TPCs [main TPCs (MTPCs)] have large dimensions ( $4\text{ m} \times 4\text{ m} \times 1.2\text{ m}$ , 90 pad rows) and provide additional momentum resolution for high-momentum particles as well as PID by  $dE/dx$  measurements with a resolution of  $\sim 4\%$ . Two time-of-flight (TOF) scintillator arrays of 891 pixels each, situated just behind the MTPCs symmetrically on either side of the beam axis, supplement PID in the momentum range from 1 to 10 GeV/c. A veto calorimeter (VCAL), which is placed further downstream along the beam and covers the projectile spectator phase-space region, is used to select event centrality. The NA49 detector is described in detail in Ref. [17]. The Pb beam had a typical intensity of  $10^4$  ions/s and impinged on a target Pb foil with a (areal) density of  $224\text{ mg/cm}^2$ . It passed through a quartz Cherenkov detector from which the start signal for the TOF measurement was obtained, and three stations of multiwire proportional chambers that measured the trajectories of individual beam particles. A minimum bias trigger was derived from the signal of a gas Cherenkov device right behind the target. Only interactions that reduce the beam charge and thus the signal seen by this detector by at least 10% are accepted. The interaction cross section thus defined is 5.7 b at both energies. The contamination by background events remaining after cuts on vertex position and quality amounts to less than 5% for the most peripheral collisions and is negligible for near-central collisions (see Ref. [18]). The resulting event ensemble was divided into five centrality classes C0, C1, C2, C3, and C4 (see Table I and Ref. [18]). The centrality selection is based on the forward-going energy of projectile spectators as measured in VCAL. Simulated events from the VENUS 4.12 Monte Carlo (MC) code [19] were used to generate realistic VCAL spectra at both energies. After cross calibration of experimental and simulated spectra for effects of the experimental trigger in the most peripheral centrality bin, the average numbers of interacting (wounded) nucleons ( $N_w$ ) were calculated for the selected cross-section fractions [20], which are identical at 40A and 158A GeV.

TABLE I. Cross-section fractions in percent centrality, average numbers of wounded nucleons ( $N_w$ ), and numbers of analyzed events for the five centrality classes at 40A and 158A GeV. Only systematic errors are quoted.

Centrality class	Centrality (%)	$\langle N_w \rangle$	Analyzed events
40A GeV			
C0	0–5	$356 \pm 1$	13 034
C1	5–12.5	$292 \pm 2$	22 971
C2	12.5–23.5	$212 \pm 3$	34 035
C3	23.5–33.5	$144 \pm 4$	32 668
C4	33.5–43.5	$93 \pm 7$	32 071
158A GeV			
C0	0–5	$357 \pm 1$	15 306
C1	5–12.5	$288 \pm 2$	23 548
C2	12.5–23.5	$211 \pm 3$	37 053
C3	23.5–33.5	$146 \pm 4$	34 554
C4	33.5–43.5	$85 \pm 7$	34 583

Thus only insignificant differences are observed in the average numbers of interacting (wounded) nucleons at both energies, except for the considered most peripheral centrality interval. We attribute this difference to the slightly different online trigger conditions.

The track-finding efficiency and  $dE/dx$  resolution were optimized by track-quality criteria. To be accepted, a track must have at least 50 (out of a maximum of 90) potential points in the MTPCs and have at least five measured and ten potential points in one of the VTPCs. Finally, tracks were required to have azimuthal angles within  $\pm 30^\circ$  with respect to the bending plane in order to minimize reconstruction inefficiencies and to optimize the accuracy of the  $dE/dx$  measurements.

### III. ANALYSIS METHOD

The protons are identified by the measurement of their specific energy loss in the relativistic rise region. As an appropriate measure of  $dE/dx$ , we calculated for each track the truncated mean of the distribution of charges measured in each pad row of the MTPCs. Their raw yields were extracted by fitting the function  $F$  [see Eq. (1) below] to the  $dE/dx$  distribution of all positively charged particles in narrow bins of total momentum  $p$  and transverse momentum  $p_T$  [21]. Antiproton yields are determined from the  $dE/dx$  distributions of all negatively charged particles with the same method at 158A GeV. At 40A GeV the antiproton statistics was very low and did not allow reliable extraction of yields. The shape of  $F$  is assumed to be the sum of Gaussians. Their parameters depend on the particle masses and the measured track lengths. We modified the Gaussian functions by means of an extra asymmetry parameter to account for tails of the Landau distributions, which are still present even after truncation.

The function  $F$  reads

$$F\left(\frac{dE}{dx}\right) = \sum_{i=d,p,K,\pi,e} A_i \frac{1}{\sum_l n_l} \sum_l \frac{n_l}{\sqrt{2\pi}\sigma_{i,l}} \times \exp\left[-\frac{1}{2}\left(\frac{e_i(p) - \hat{e}_i(p)}{(1 \pm \delta)\sigma_{i,l}}\right)^2\right]. \quad (1)$$

Here  $\frac{dE}{dx}$  (abbreviated  $e$ ) is the measure of specific ionization, and  $\hat{e}$  is its most probable value. The other parameters of the function are as follows: (i)  $A_i$  is the raw yield of the particle  $i$  under consideration in a given phase-space bin. (ii)  $n_l$  is the number of tracks in a given track length interval  $l$ . The second sum together with the normalization  $\sum_l n_l$  forms the weighted average of the track ensembles in each phase-space interval. (iii)  $\sigma_{i,l}$  is the width for the asymmetric Gaussian of particle type  $i$  in length interval  $l$ . (iv)  $\delta$  is the asymmetry parameter.

The amplitude parameters  $A_i(p, p_T)$  were determined by a maximum likelihood fit to the  $dE/dx$  histogram in each  $p, p_T$  bin. The peak positions  $\hat{e}_i(p)$  are considered to be  $p_T$  independent and were determined by fits to the  $p_T$ -integrated distributions in all  $p$  bins. The fitted peak positions  $\hat{e}_i(p)$  for  $\pi^+$ ,  $K^+$ , and  $p$  are compared to a parametrization of the momentum dependence of the most probable energy loss determined for the NA49 detector in Fig. 1(a). The relative differences between fitted (anti)proton positions and

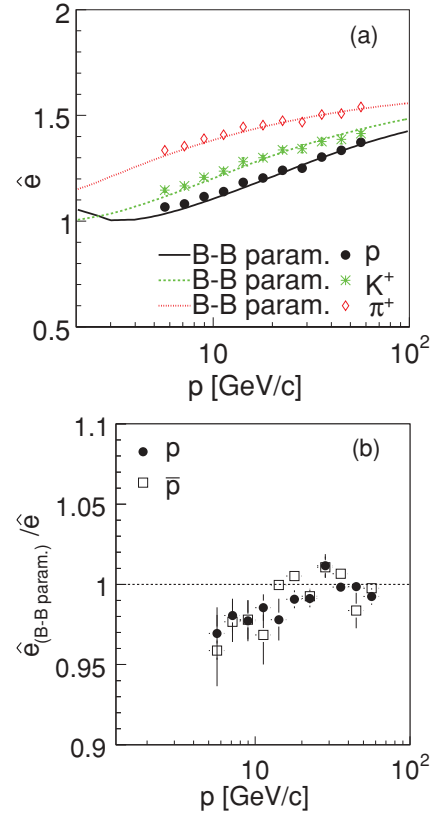


FIG. 1. (Color online) (a) The most probable specific energy loss  $\hat{e}$  for particle species  $\pi^+$ ,  $K^+$ , and  $p$  as a function of total momentum  $p$ . The points show results extracted from data, whereas the lines indicate the Bethe-Bloch parametrizations optimized for the NA49 measurement. (b) The ratios of the Bethe-Bloch parametrizations ( $\hat{e}_{B-B \text{ param.}}$ ) to  $\hat{e}$  from fits to the data are shown as a function of laboratory momentum.

the Bethe-Bloch parametrization are smaller than 5% [see Fig. 1(b)]. We have verified that the peak positions do not depend on centrality. The widths of the Gaussians ( $\sigma_{i,l}$ ) depend on the particle type  $i$  and on the track length  $L$  according to  $\sigma_{i,l} = \sigma \cdot (\hat{e}_i/e_\pi)^\alpha (1/\sqrt{L})$ . The exponent  $\alpha$  ( $\approx 0.625$ ) was extracted from simultaneous fits to  $m^2$  distributions from TOF and to  $dE/dx$  distributions from the TPCs [21]. The momentum-averaged widths  $\langle \sigma \rangle$  were determined for each centrality bin by fits to the data in the whole  $p$  range. These momentum averaged widths  $\langle \sigma \rangle$  turned out to be  $\sim 4\%$  for each centrality bin.  $\delta$  was studied by fits with the asymmetric Gaussians. Because it did not show any significant variation with centrality, total, and transverse momentum [13], this parameter was fixed to a constant value (0.071). The total number of fit parameters for each  $p, p_T$  bin is 9. The raw yields were transformed from a fine grid in  $\log(p), p_T$  to a coarser grid in  $y, p_T$ . Examples of the transformed results for centrality class C2 are shown in Fig. 2.

#### A. Acceptance and efficiency

The raw particle yields have to be corrected for losses owing to tracks that do not pass through the detectors or that

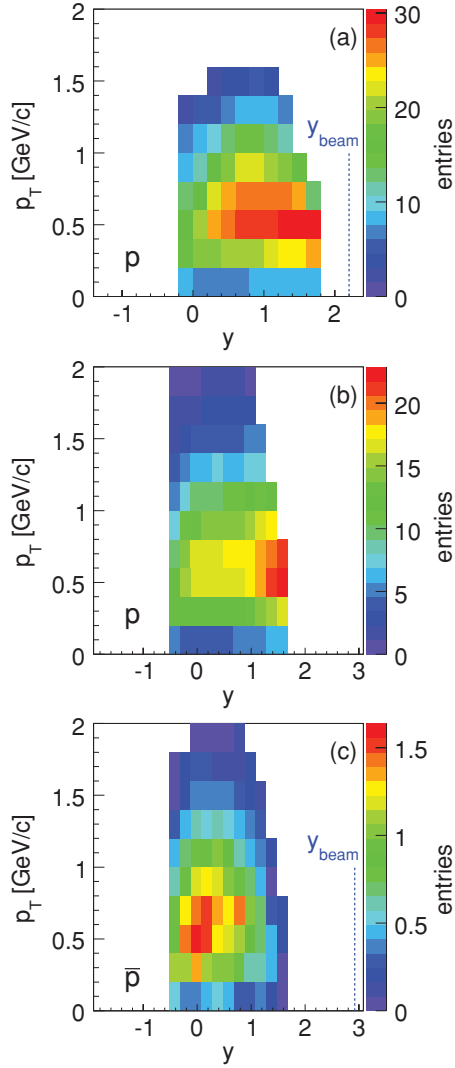


FIG. 2. (Color online) Raw yields per event of protons at (a) 40A GeV, (b) protons, and (c) antiprotons at 158A GeV are shown as a function of c.m. rapidity  $y$  and  $p_T$  for centrality class C2.

do not fulfill the acceptance criteria (acceptance losses) and tracks that are not properly reconstructed (efficiency losses). The acceptance was calculated by generating a sample of (anti)protons with flat distributions in transverse momentum and rapidity. The generated particles were propagated through the detectors (and the magnetic field) using the programs provided in the GEANT 3.21 [22] package. Along the resulting trajectories, realistic detector signals were generated and processed in exactly the same way as the experimental data. The ratio of generated to accepted particle tracks in each  $y$ ,  $p_T$  bin is the acceptance correction factor. In addition to the well-defined corrections necessary to correct for the limited and constrained acceptance, the raw spectra may be subject to losses owing to detector occupancy and thus centrality-dependent inefficiencies. These losses were minimized by restricting the analysis to tracks with azimuthal emission angles within  $\pm 30^\circ$  with respect to the bending plane and in the bending direction. The remaining losses were determined by the following procedure: Ten GEANT generated (anti)proton

tracks and their signals were embedded into raw data of real events. Only those tracks are embedded that pass all acceptance criteria. These modified events are reconstructed with the standard reconstruction chain. The ratio of all generated tracks to those reconstructed constitutes the applied correction factor for reconstruction inefficiencies. The resulting efficiencies vary with centrality by less than 5% and are over 95% in most  $y$ ,  $p_T$  bins. In the further analysis, the bin size in rapidity of the antiproton spectra [see Fig. 2(c)] was increased from 0.2 to 0.4 units in order to reduce the statistical errors.

### B. Feed-down corrections

The measured (anti)proton yield contains (anti)protons from weak hyperon decays, namely, of the  $\Lambda$  ( $\bar{\Lambda}$ ), the  $\Sigma^0$  ( $\bar{\Sigma}^0$ ), and the  $\Sigma^+$  ( $\bar{\Sigma}^-$ ). The (anti)proton contribution from  $\Sigma^+$  ( $\bar{\Sigma}^-$ ) decays is determined by scaling the estimated feed-down correction coming from  $\Lambda$  ( $\bar{\Lambda}$ ) by the ratio  $\Lambda/\Sigma^+$  ( $\bar{\Lambda}/\bar{\Sigma}^-$ ) derived from a statistical hadron gas model [23], thus assuming the same phase-space distributions for  $\Lambda$  ( $\bar{\Lambda}$ ) and  $\Sigma^+$  ( $\bar{\Sigma}^-$ ) hyperons. To determine the feed-down correction  $n_{fd}$  from  $\Lambda$  ( $\bar{\Lambda}$ ) in each measured phase-space bin, we used a similar procedure as for the efficiency calculation.  $\Lambda$  ( $\bar{\Lambda}$ ) were generated according to distributions measured by NA49 [16,24] and embedded into real events. Those (anti)protons from embedded  $\Lambda$  ( $\bar{\Lambda}$ ) decays, which are reconstructed and accepted by the track selection cuts as such, have to be subtracted from the (anti)proton yield after proper normalization per event [see Eq. (2)]. In Refs. [16] and [24] the measured  $\Lambda$  ( $\bar{\Lambda}$ ) include the  $\Lambda$  ( $\bar{\Lambda}$ ) from electromagnetic decays of  $\Sigma^0$  and  $\bar{\Sigma}^0$ . The feed-down correction is given by

$$n_{fd}(y, p_T) = \frac{N_{\Lambda(\bar{\Lambda})}^{\text{found}}(y, p_T)}{N_{\Lambda(\bar{\Lambda})}^{\text{sim}}(y, p_T)} Y_{\text{tot}}(y, p_T), \quad (2)$$

where  $N_{\Lambda(\bar{\Lambda})}^{\text{found}}(y, p_T)$  is the average number of reconstructed (anti-)protons per event from embedded  $\Lambda$  ( $\bar{\Lambda}$ ) decays,  $N_{\Lambda(\bar{\Lambda})}^{\text{sim}}(y, p_T)$  is the number of simulated  $\Lambda$  ( $\bar{\Lambda}$ ), and  $Y_{\text{tot}}(y, p_T)$  is the multiplicity of  $\Lambda$  ( $\bar{\Lambda}$ ) in the phase-space interval from Refs. [16] and [24] scaled for the contributions from  $\Sigma^+$  ( $\bar{\Sigma}^-$ ). The lowest and the two highest rapidity bins in the 40A GeV data [see Fig. 2(a)] were removed owing to low statistics in too many  $p_T$  bins.

### C. Systematic errors

One of the sources for systematic errors is the uncertainty in the procedure of unfolding the  $dE/dx$  distributions. Studies of the sensitivity to small changes of the fit parameters showed that the systematic errors are of the same order as the statistical errors. The largest contribution to the systematic error was traced to the deviations of the peak positions from the predicted values (see Fig. 1). They reach up to 4% in the yields in the low-momentum bins. The next source of systematic errors is the uncertainty related to acceptance, inefficiencies, and feed-down correction calculations. To estimate the magnitude of these errors, cut parameters were varied such that significantly different correction factors were obtained. The resulting final



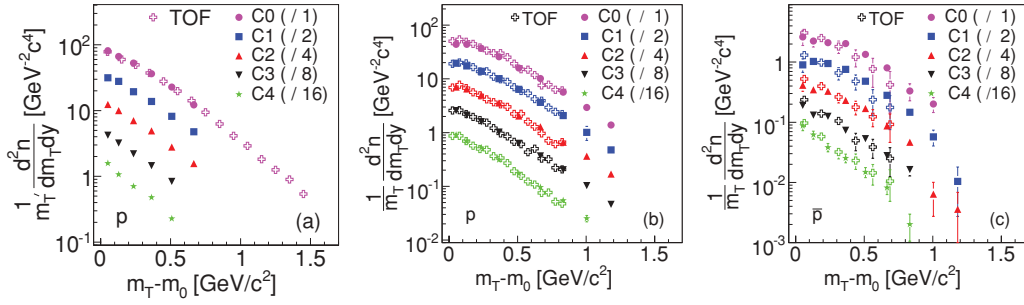


FIG. 3. (Color online) Invariant  $m_T$  spectra of protons at (a) 40A GeV and (b) 158A GeV as well as antiprotons at (c) 158A GeV for five centrality bins in Pb + Pb collisions. The respective c.m. rapidity intervals are  $-0.02 < y < 0.18$ ,  $-0.12 < y < 0.08$ ,  $-0.12 < y < 0.08$ . The data at different centralities are scaled down by the factors indicated in the figures. The new NA49 measurements (filled symbols) are compared, whenever available, to results of an earlier analysis using TOF information for particle identification [6] (open symbols). Only statistical errors are shown if larger than the symbol size. For the systematic errors, see Sec. III C.

results varied only within the statistical errors. Overall it appears that the systematic uncertainties resulting from the correction procedures are of the order of 3% or less.

The determination of the rapidity density distributions required extrapolations of the transverse-momentum distributions. Their contribution is negligible for most of the rapidity bins except the rapidity bins  $y \geq 1.2$ , where the extrapolation factors reached values of 1.3. Single and double exponentials were used to describe the shape of the transverse-momentum distributions in this region. The resulting differences of  $p_T$ -integrated yields are smaller than 2%. Finally, the results from the  $dE/dx$  analysis in this paper and the TOF results [6] agree mostly within 5% in the common acceptance region at all centralities except for some of the two lowest  $m_T$  points, which deviate up to 20% in the 158A GeV data. These differences can be traced to the feed-down corrections, which relied on

different (older) parametrizations used for the MC input of (anti)lambda phase-space distributions in Ref. [6], but are based on recent measured data in this analysis (see above). However, this uncertainty has only a small effect on the value of  $dn/dy$ . We conclude from these studies that each data point carries a systematic uncertainty of  $\sim 7\%$ .

## IV. RESULTS AND COMPARISON WITH MODELS

### A. Transverse-momentum spectra

Transverse-momentum distributions of (anti)protons were determined in ten (11) bins of rapidity at 40A GeV (158A GeV), as shown in Fig. 2. The range covered in transverse momentum extends from  $p_T$  equal zero to 0.8 GeV/c at high rapidity and up to 1.5 GeV/c (2 GeV/c) for

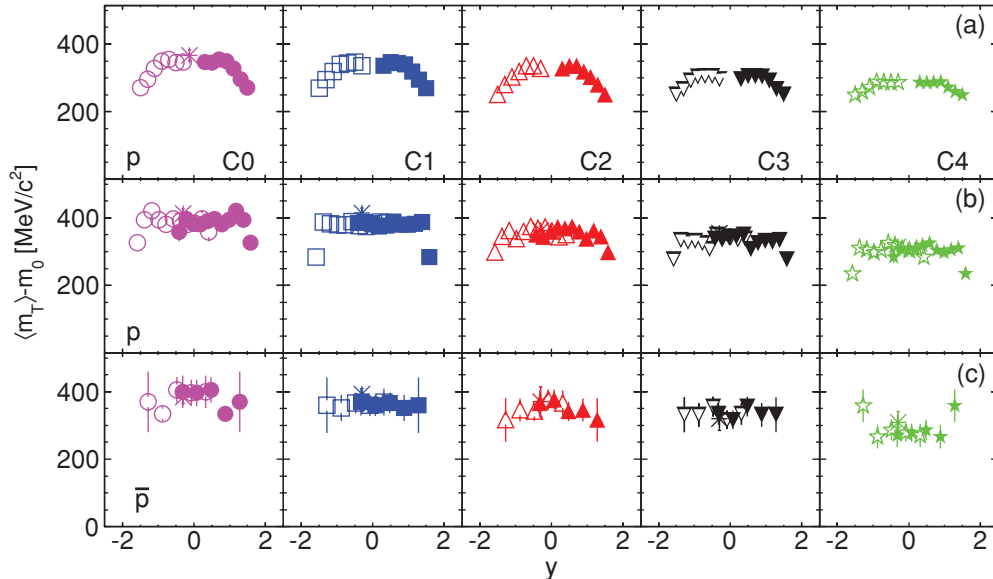


FIG. 4. (Color online)  $\langle m_T \rangle - m_0$  for (anti)protons as function of rapidity for five centrality intervals in Pb + Pb collisions. We show in the upper row (a) protons at 40A GeV, in the middle row (b) protons at 158A GeV, and in the lower row (c) antiprotons at 158A GeV. The open symbols are obtained by reflection at midrapidity. Asterisks refer to results of an earlier analysis using TOF information for particle identification [6]. Only statistical errors are shown (if larger than the symbol size). For the systematic errors, see Sec. III C.

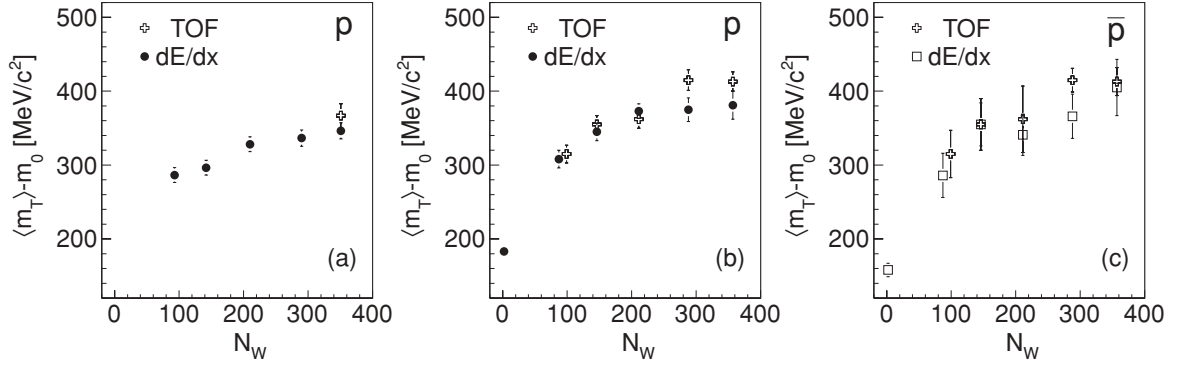


FIG. 5.  $\langle m_T \rangle - m_0$  near midrapidity as function of  $\langle N_w \rangle$  in Pb + Pb collisions. The leftmost panel (a) shows the proton data at 40A GeV, the middle panel (b) the proton data at 158A GeV, and the right panel (c) the antiproton data at 158A GeV. The results of this analysis (labeled  $dE/dx$ ) are compared to previously published Pb + Pb data (labeled TOF) [6]. The ordinate has a suppressed zero. Only statistical errors are shown (if larger than the symbol size). For the systematic errors, see Sec. III C.

$0.0 < y < 1.0$  at 40A GeV (158A GeV). Whenever necessary, the  $p_T$  spectra were extrapolated to 2 GeV/c (neglecting contributions at higher transverse momenta that have been accounted for in the systematic uncertainties) by taking the mean of fits to the data based on a single exponential and a superposition of two exponential functions. At 40A GeV, the extrapolation of the two bins around midrapidity were performed with the functional form obtained from the adjacent rapidity bin because of low statistics in the  $p_T$  distributions. Using these extrapolations,  $p_T$  integrated yields ( $dn/dy$ ) and mean  $m_T$  values ( $\langle m_T \rangle - m_0$ ) as function of rapidity were calculated (see below). Midrapidity invariant  $m_T$  spectra ( $1/m_T d^2n/(dm_T dy)$ ) at 40A and 158A GeV are compared in Fig. 3 with the results of a TOF-based analysis published previously [6]. We find agreement within errors except for deviations at low  $p_T$ , which have been addressed in the previous section.

Because the shapes of all invariant  $m_T$  spectra deviate significantly from single exponentials, we choose  $\langle m_T \rangle - m_0$  instead of the inverse slope parameter of the transverse-mass spectra to study the transverse activity as function of rapidity. Figure 4 shows  $\langle m_T \rangle - m_0$  of protons at 40A GeV (upper row) and 158A GeV (middle row), and antiprotons at 158A GeV (lower row) as function of c.m. rapidity. In the latter, the bin size in rapidity was doubled to reduce the statistical errors on the data points. The  $\langle m_T \rangle - m_0$  values near midrapidity are plotted in Fig. 5 as function of centrality. Also shown are the data points from the TOF analysis [6] and recent results from p + p interactions at the same energy [25]. A clear increase of  $\langle m_T \rangle - m_0$  by  $\sim 30\%$  is observed when comparing the values obtained in the most peripheral with the most central event sample. The increase is close to a factor of 2 when the results on p + p interactions are taken as a reference. Similar observations have been made by NA49 for data on hyperons [24].

### B. Rapidity spectra

The rapidity densities  $dn/dy$  in each rapidity interval were obtained by summing the yields in the measured  $p_T$  interval and the integrals of the extrapolation function above the highest measured  $p_T$  bin. The additive correction was calculated as

the average of the single and the double exponentials in the unmeasured  $p_T$  region. The contributions of the extrapolation to  $dn/dy$  are mostly of order of 3% (6%) for protons and below 5% for antiprotons at 158A GeV (40A GeV) and contribute negligibly to the errors of the integrals. These extrapolations reach up to 25%, close to the limits of the accepted rapidity region.

The rapidity spectra of protons at (a) 40A GeV and net protons at (b) 158A GeV are presented in Fig. 6 for five different centrality selections (C0–C4). We included the  $dn/dy$

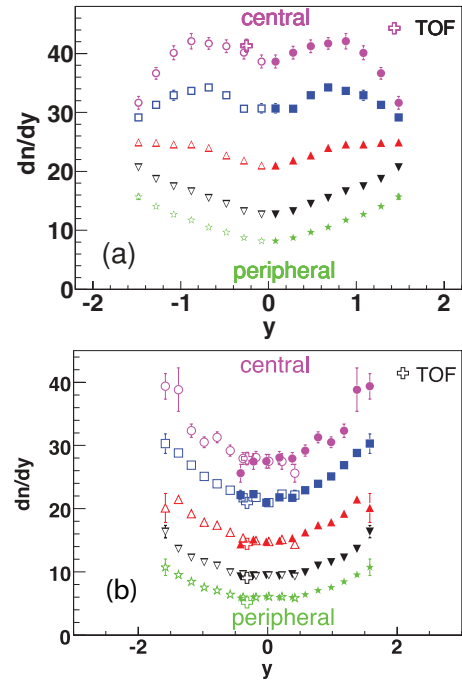


FIG. 6. (Color online)  $dn/dy$  of (net) protons for five different centralities. We show in (a) the proton distributions at 40A GeV and in (b) the difference between proton and antiproton spectra (i.e., the net-proton spectra) at 158A GeV. The open symbols are obtained by reflection at midrapidity. Also shown are the results from an earlier analysis labeled TOF [6]. Only statistical errors are shown (if larger than the symbol size). For the systematic errors, see Sec. III C.

TABLE II. Proton rapidity densities  $dn/dy$  at five different centralities and 40A GeV. The quoted errors are statistical. For the systematic errors, see Sec. III C.

	$dn/dy$ (C0)	$dn/dy$ (C1)	$dn/dy$ (C2)	$dn/dy$ (C3)	$dn/dy$ (C4)
$-0.02 \leq y \leq 0.18$	$38.64 \pm 1.11$	$30.69 \pm 0.79$	$21.01 \pm 0.51$	$12.69 \pm 0.33$	$8.19 \pm 0.20$
$0.18 \leq y \leq 0.38$	$40.15 \pm 1.07$	$30.63 \pm 0.75$	$21.86 \pm 0.51$	$13.26 \pm 0.34$	$8.74 \pm 0.22$
$0.38 \leq y \leq 0.58$	$41.23 \pm 1.08$	$32.93 \pm 0.70$	$22.72 \pm 0.51$	$14.49 \pm 0.34$	$9.68 \pm 0.23$
$0.58 \leq y \leq 0.78$	$41.72 \pm 0.98$	$34.24 \pm 0.74$	$24.01 \pm 0.52$	$15.48 \pm 0.35$	$10.51 \pm 0.23$
$0.78 \leq y \leq 0.98$	$42.08 \pm 1.32$	$33.65 \pm 0.72$	$24.57 \pm 0.49$	$16.64 \pm 0.37$	$11.71 \pm 0.24$
$0.98 \leq y \leq 1.18$	$40.11 \pm 1.19$	$32.91 \pm 0.85$	$24.58 \pm 0.50$	$17.48 \pm 0.38$	$12.71 \pm 0.28$
$1.18 \leq y \leq 1.38$	$36.64 \pm 0.98$	$31.29 \pm 0.73$	$24.84 \pm 0.53$	$18.70 \pm 0.42$	$14.06 \pm 0.33$
$1.38 \leq y \leq 1.58$	$31.63 \pm 1.09$	$29.16 \pm 0.76$	$24.94 \pm 0.56$	$20.69 \pm 0.51$	$15.69 \pm 0.48$

values obtained from the TOF analysis (asterisks) published earlier by NA49 [6] for comparison. At both energies the yields increase with centrality. No change in shape is apparent at 158A GeV beam energy, whereas at 40A GeV the form of the  $dn/dy$  distribution evolves from a parabolic shape near to midrapidity ( $|y| < 1$ ) in semiperipheral to a double hump structure in central collisions. The  $dn/dy$  values of protons at 40A GeV are given in Table II, those for protons at 158A GeV in Table III, and for antiprotons in Table IV.

The trends in the evolution of the rapidity distributions are seen best when the spectra are divided by the number of wounded nucleons, as shown in Fig. 7. The proton spectra at 158A GeV (middle panel) change slightly. The normalized yields (at midrapidity) increase by  $\sim 15\%$  from 0.065 to 0.075 when going from semiperipheral to central collisions. At 40A GeV the scaled yields at midrapidity increase by 25% from 0.085 to 0.11 from semiperipheral to central collisions. As to the shape, it seems that with decreasing centrality, additional protons populate the region  $|y| < (y_{\max} - 1.2)$ . The shape of the antiproton distributions at 158A GeV resembles a Gaussian and does not change with centrality. The integrated and midrapidity yields normalized by  $\langle N_w \rangle$  decrease by 20% with increasing centrality.

We present the dependences on centrality of the normalized antiproton multiplicity and of the width of their rapidity distribution in Fig. 8, together with NA49 data from elementary p + p interactions [25], both at 158A GeV. The mean

multiplicities (total yield per event) of antiprotons for different centralities were calculated by integrating the measured rapidity spectra and by extrapolating into the unmeasured regions assuming a Gaussian shape (see Fig. 7). The magnitude of the corresponding extrapolation factors are in the range from 5% to 10%. A double Gaussian fit is used to estimate the systematic errors of the extrapolation into the high  $y$  region. The antiproton multiplicity normalized to  $\langle N_w \rangle$ , shown in the upper panel of Fig. 8, increases by nearly a factor 1.5 when going from midcentral Pb + Pb to inelastic p + p collisions, and stays constant from midcentral to central Pb + Pb collisions. Although the properly weighted average of yields in p + p and n + n collisions would be the appropriate reference for this comparison, we consider the p + p midrapidity yield to be a good approximation. It is interesting to note that the antiproton multiplicity (from Ref. [24]<sup>1</sup>), also shown in Fig. 8(a), exhibits a centrality dependence similar to the one of the antiprotons except for the most peripheral bin and the p + p data points. The lower panel of Fig. 8 shows the centrality dependence of the widths of the rapidity distributions for antiprotons and antilambdas (from Ref. [24]<sup>1</sup>). These widths are nearly the same for  $\bar{p}$  and  $\bar{\Lambda}$  and are rather independent of centrality except again for the most peripheral bin and the results from p + p collisions.

<sup>1</sup>The data on  $\bar{\Lambda}$  yield and rapidity width in p + p interactions are preliminary NA49 results that are subject to 7% systematical errors.

TABLE III. Proton rapidity densities  $dn/dy$  at five different centralities and 158A GeV. The quoted errors are statistical. For the systematic errors, see Sec. III C.

	$dn/dy$ (C0)	$dn/dy$ (C1)	$dn/dy$ (C2)	$dn/dy$ (C3)	$dn/dy$ (C4)
$-0.52 \leq y \leq -0.32$	$25.63 \pm 1.41$	$22.17 \pm 0.74$	$14.36 \pm 0.43$	$9.28 \pm 0.30$	$5.84 \pm 0.21$
$-0.32 \leq y \leq -0.12$	$27.49 \pm 1.24$	$22.32 \pm 0.61$	$15.14 \pm 0.38$	$9.46 \pm 0.25$	$6.03 \pm 0.18$
$-0.12 \leq y \leq 0.08$	$27.51 \pm 1.09$	$20.97 \pm 0.52$	$14.79 \pm 0.33$	$9.46 \pm 0.23$	$6.07 \pm 0.19$
$0.08 \leq y \leq 0.28$	$28.07 \pm 1.01$	$21.81 \pm 0.51$	$14.96 \pm 0.31$	$9.34 \pm 0.21$	$5.98 \pm 0.16$
$0.28 \leq y \leq 0.48$	$27.93 \pm 0.94$	$21.74 \pm 0.52$	$15.35 \pm 0.30$	$9.64 \pm 0.21$	$5.96 \pm 0.15$
$0.48 \leq y \leq 0.68$	$29.20 \pm 0.89$	$22.91 \pm 0.50$	$16.27 \pm 0.30$	$9.92 \pm 0.23$	$6.39 \pm 0.16$
$0.68 \leq y \leq 0.88$	$31.30 \pm 0.88$	$23.96 \pm 0.49$	$17.4 \pm 0.31$	$10.97 \pm 0.23$	$7.05 \pm 0.17$
$0.88 \leq y \leq 1.08$	$30.51 \pm 0.85$	$25.10 \pm 0.49$	$17.87 \pm 0.32$	$11.53 \pm 0.24$	$7.55 \pm 0.19$
$1.08 \leq y \leq 1.28$	$32.35 \pm 1.05$	$26.88 \pm 0.57$	$19.22 \pm 0.39$	$12.25 \pm 0.26$	$8.43 \pm 0.20$
$1.28 \leq y \leq 1.48$	$38.84 \pm 3.43$	$28.82 \pm 0.58$	$21.46 \pm 0.43$	$13.63 \pm 0.28$	$9.52 \pm 0.22$
$1.48 \leq y \leq 1.68$	$39.35 \pm 2.00$	$30.30 \pm 1.55$	$20.13 \pm 2.30$	$16.38 \pm 0.98$	$10.73 \pm 1.31$



TABLE IV. Antiproton rapidity densities  $dn/dy$  at five different centralities and 158A GeV. The quoted errors are statistical. For the systematic errors, see Sec. III C.

	$dn/dy$ (C0)	$dn/dy$ (C1)	$dn/dy$ (C2)	$dn/dy$ (C3)	$dn/dy$ (C4)
$-0.52 \leq y \leq -0.12$	$1.61 \pm 0.13$	$1.37 \pm 0.09$	$0.92 \pm 0.06$	$0.78 \pm 0.05$	$0.51 \pm 0.04$
$-0.12 \leq y \leq 0.28$	$1.75 \pm 0.12$	$1.37 \pm 0.08$	$1.06 \pm 0.05$	$0.80 \pm 0.04$	$0.55 \pm 0.03$
$0.28 \leq y \leq 0.68$	$1.76 \pm 0.11$	$1.43 \pm 0.07$	$0.96 \pm 0.05$	$0.70 \pm 0.04$	$0.49 \pm 0.03$
$0.68 \leq y \leq 1.08$	$1.31 \pm 0.10$	$1.11 \pm 0.07$	$0.80 \pm 0.05$	$0.54 \pm 0.038$	$0.36 \pm 0.03$
$1.08 \leq y \leq 1.48$	$0.60 \pm 0.10$	$0.57 \pm 0.09$	$0.37 \pm 0.05$	$0.21 \pm 0.03$	$0.31 \pm 0.06$

Net-proton rapidity distributions for all five centralities are obtained by subtracting the antiproton distributions from those of the protons. The result at 158A GeV for central collisions (bin C0) is compared to data published earlier [3] in Fig. 9. The differences between the two measurements can be traced back to different analysis methods. The earlier analysis used a method in which distributions of negatively charged particles were subtracted from those of the positively charged ones, assuming the proton mass for all particles. The resulting distributions were corrected for the then unmeasured differences between  $\pi^+$  and  $\pi^-$ , as well as  $K^+$  and  $K^-$  yields by means of model calculations and detector simulations (see Ref. [3]). The resulting systematic error was quoted to be below 10%. Here we identify the protons and antiprotons directly by means of their specific energy loss in the MTPCs. An additional difference between the two analyses is the feed-down correction. In the former analysis it had to be quantified with the help of model predictions that later turned out to underpredict the hyperon yields. Also, the phase-space distributions of hyperons were not yet known at that time. Under such conditions it was impossible to quantify the resulting systematic error, because too little was known

about hyperon production in heavy-ion collisions at SPS energies. The new results are therefore more reliable owing to the smaller and better determined corrections, leading to smaller systematic uncertainties. However, the two results are consistent within the large systematic errors of the analysis in Ref. [3].

### C. Model comparisons and conclusions

Net-proton spectra are compared with HSD [26] and UrQMD-2.3 [27] model calculations. Before addressing possible differences between the model results and Pb+Pb collision data, we check how well the models reproduce the rapidity distribution of net protons in p+p interactions. It is important to note here that the model calculations include also elastic scattering, whereas the experimental data represent inelastic interactions only. Figure 10 reveals significant differences between the models and the experimental data. First, UrQMD [27] has more stopping than HSD [26] with a similar shape as the data, but a significantly higher yield at midrapidity. Second, HSD reproduces the midrapidity yield but fails to reproduce the shape. These shortcomings render

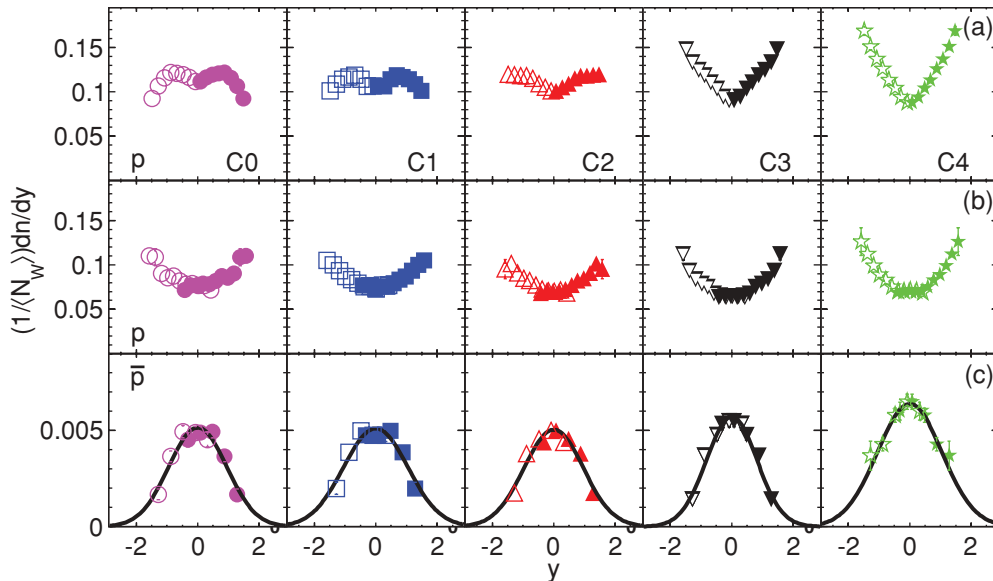


FIG. 7. (Color online) Rapidity density distributions per wounded nucleon are shown for protons at 40A GeV (top row), protons at 158A GeV (middle row), and antiprotons at 158A GeV (bottom row) for five centralities in Pb + Pb collisions. The open symbols are obtained by reflection about midrapidity. The solid lines represent results of single Gaussian fits. For the statistical errors see Fig. 6. For the systematic errors, see Sec. III C.

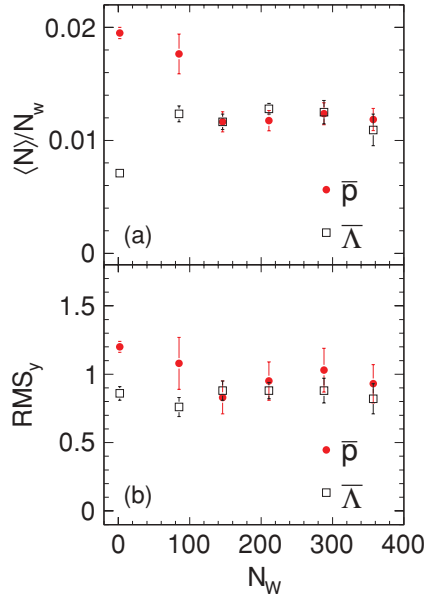


FIG. 8. (Color online) The total multiplicities (per wounded nucleon) of  $\bar{p}$  and  $\bar{\Lambda}$  (upper panel) and the  $RMS_y$  widths of the  $dn/dy$  distributions of  $\bar{p}$  and  $\bar{\Lambda}$  (lower panel) for five centralities as a function of the number of wounded nucleons  $\langle N_w \rangle$  in Pb + Pb collisions at 158A GeV. The  $\bar{\Lambda}$  data are from Ref. [24]. Also shown are results on antiprotons and  $\bar{\Lambda}$  obtained from p + p interactions (for references see the text). Only statistical errors are shown (if larger than the symbol size). For the systematic errors, see Sec. III C.

comparisons to Pb + Pb data questionable. The comparison is shown nevertheless in Fig. 11 for 40A GeV and in Fig. 12 for 158A GeV, in which the rapidity density distributions are divided by the average number of wounded nucleons  $\langle N_w \rangle$ . Note that antiprotons were not subtracted in the 40A GeV data, because their yield is negligibly small compared to the proton yield ( $<1\%$  at midrapidity). Overall, we observe fair agreement between the HSD model calculation and the data in the rapidity region covered by the NA49 measurements. Larger disagreements are seen for the UrQMD predictions. The differences can be attributed either to known differences between the models (see below) or to the deficiencies in describing proton distributions in elementary p + p interactions. The HSD [26] calculations always describe the data better than UrQMD [27] calculations. These significant differences in the rapidity distributions between HSD and UrQMD are owing to a different definition of “formed” and “unformed” hadrons. In HSD, a hadron is considered as “formed” only if the energy density (in the surrounding cell) drops below a critical value, which is taken to be  $1 \text{ GeV}/\text{fm}^3$ , in line with results from lattice quantum chromodynamics (QCD) on the critical energy density for deconfinement. Otherwise the hadron is considered as “unformed” and unable to interact with other hadrons. This energy density criterion is not included in UrQMD, which leads therefore to a substantial overestimate of the energy loss of participant nucleons in collisions in which high-energy densities are reached [26].

In Pb + Pb collisions at 158A GeV we observe a parabolic shape near to midrapidity ( $|y| < 1$ ) that is similar to the one seen in inelastic p + p interactions as well as in HSD calcu-

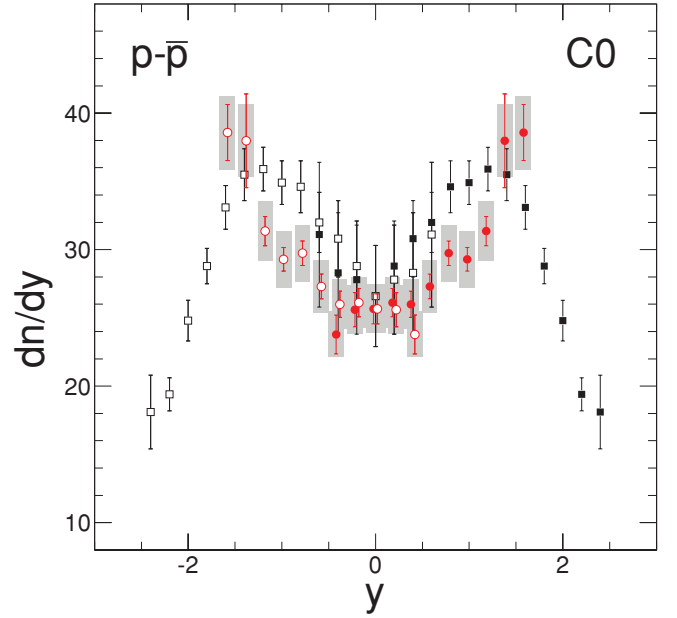


FIG. 9. (Color online) The net-proton rapidity distribution at 158A GeV for centrality bin C0 is compared with previously published data [3]. The full circles indicate results from the analysis presented in this paper, whereas the full squares show the previously published data. The open points result from reflection of the data points at midrapidity. The shaded bars represent the systematic uncertainties. Error bars represent statistical errors.

lations. This can be attributed to the exponential decrease of the proton yield toward midrapidity (according to  $\exp[-(y - y_{\text{beam}})]$ ), which in turn results from the approximately flat probability density distribution as a function of Feynman  $x$  [1]. At 40A GeV the rapidity distributions are similar to those at

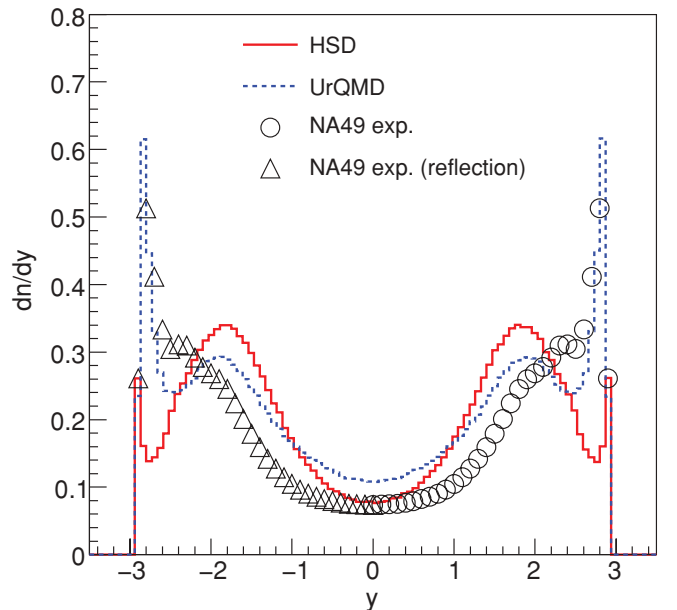


FIG. 10. (Color online) Rapidity distribution of net protons from p + p collisions at 158 GeV/c beam momentum [25]. The solid line represents the HSD [26] and the dashed line the UrQMD [27] calculation.

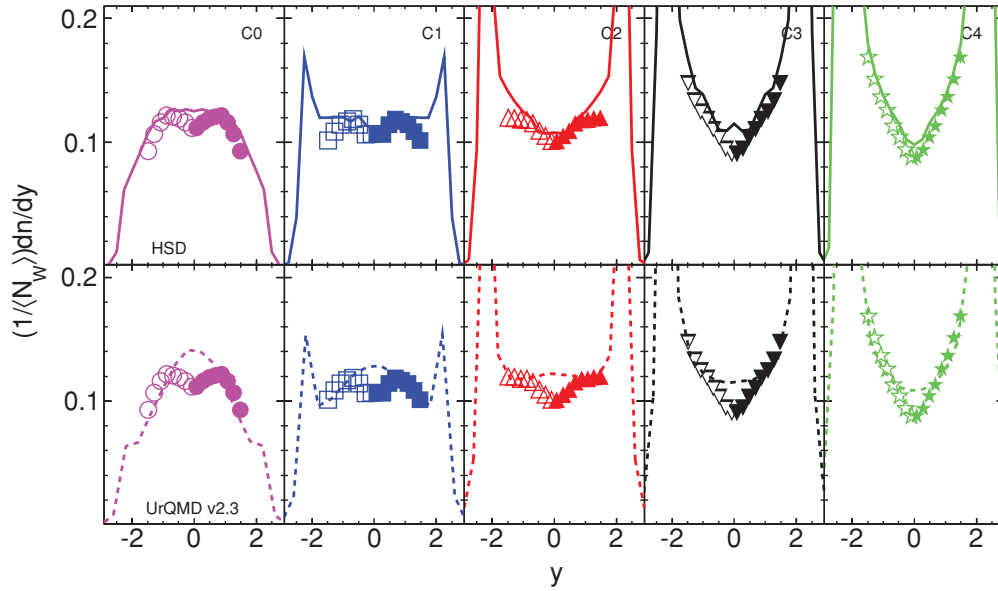


FIG. 11. (Color online) The rapidity distributions scaled with  $1/\langle N_w \rangle$  of net protons for five different centralities at 40A GeV are shown together with results of HSD (top) [26] and UrQMD (bottom) [27] calculations. For the statistical errors see Fig. 6. For the systematic errors, see Sec. III C.

158A GeV for more peripheral collisions, while they develop a double-hump structure for central collisions. The normalized midrapidity yield increases by  $\sim 25\%$  at 40A GeV and 10% at 158A GeV from the most peripheral to the most central collisions, in line with findings in earlier analyses of proton yields at midrapidity [6] and recent results on hyperons [24]. HSD calculations reproduce this trend quantitatively.

The significant differences between the proton distributions at 40A GeV and 158A GeV are at least partly owing to the differences in experimental acceptances at the two energies.

The change in shape that occurs away from midrapidity at 40A GeV is probably also present at the higher energy, however, in a range  $|y| < (y_{\text{max}} - 1.2)$ , which is outside the NA49 acceptance. Finally, the integral of the normalized net-proton distributions over the measured region increases by 8% at 40A GeV and by 5% at 158A GeV with decreasing centrality. Although this variation is not significant by itself, the results from the model calculations, in which the coverage extends from target to beam rapidity (see Figs. 11 and 12), confirm the trend. It seems that the spectrum of net protons contains,

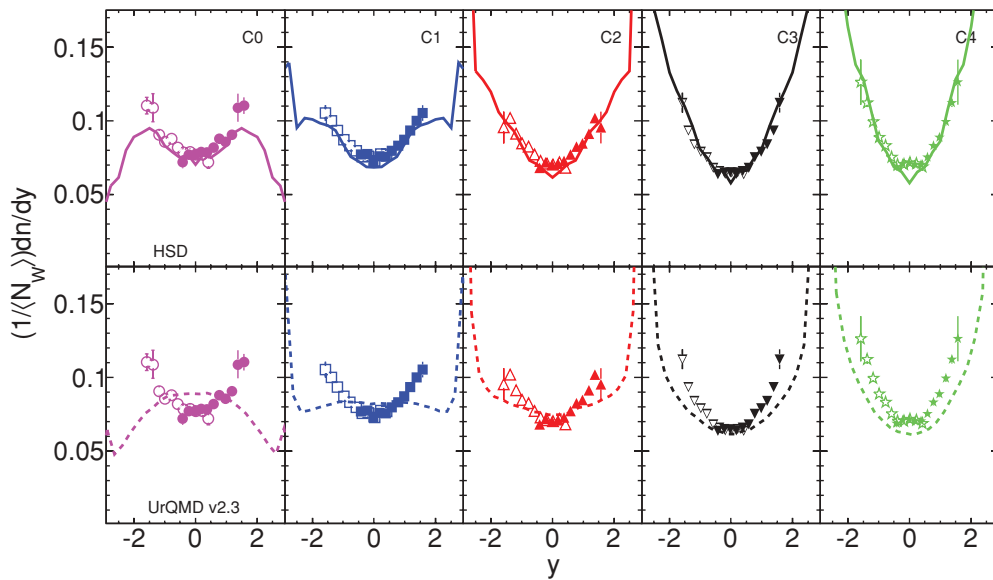


FIG. 12. (Color online) The rapidity distributions scaled with  $1/\langle N_w \rangle$  of net protons for five different centralities at 158A GeV are shown together with results of HSD (top) [26] and UrQMD (bottom) [27] calculations. For the statistical errors see Fig. 6. For the systematic errors, see Sec. III C.

with increasing impact parameter, more and more nucleons that do not stem from the nuclear overlap region specified in the Glauber model (which we call wounded nucleons). The origin of these extra nucleons could be elastic and inelastic  $N + N_{\text{spectator}}$  and meson +  $N_{\text{spectator}}$  interactions ( $N$  stands for nucleon), which boost or slow down the (spectator) nucleons, changing their status from spectators to pseudoparticipants. Because there is no way to separate pseudoparticipants from wounded nucleons in the experimental data, it is difficult to draw conclusions on nuclear stopping from the study of net-proton spectral shapes in centrality-selected Pb + Pb collisions. On the other hand, this spectator contribution seems to be absent in the hyperon rapidity distributions [24], thus the, e.g., meson +  $N_{\text{spectator}}$  interactions are not violent enough to produce hyperons.

## V. SUMMARY

The NA49 collaboration analyzed proton and antiproton spectra in 40A and 158A GeV Pb + Pb reactions covering the 43.5% most central collisions. In the transverse-mass spectra no strong variation with centrality is discernible, but the average  $m_T$  increases by  $\sim 20\%$  from peripheral to central collisions. The rapidity distributions at 158A GeV have a common concave shape [Fig. 6(b)], which, however, gets shallower with increasing centrality, best seen if normalized to the number of participants as shown in Fig. 7. The rapidity distributions at 40A GeV, on the contrary, exhibit a strong centrality dependence starting with a concave or V-shaped structure at large impact parameters, which turns into a symmetric double-hump shape for more central collisions. The minimum at the center persists at all centralities. Sizable contributions from nonparticipants in the rapidity range  $|y| < (y_{\text{beam}} - 1.2)$  are observed, which are probably owing to secondary interactions of produced particles in spectator matter. Thus rapidity loss analyses of net-proton spectra in nucleus-nucleus collisions have to account for this unwanted component of the spectrum. The midrapidity yield normalized to the number of participants varies only by 10% (5%) with centrality at 40A GeV (158A GeV), reaching its maximum for the most central collisions. As expected, it decreases when going from

40A GeV to 158A GeV (by 25%). These findings may be compared to the corresponding data from AGS experiment E917 extracted from Ref. [2], using Ref. [28] to compute the number of participants. We find approximately a factor of 2 higher (normalized) yields at midrapidity with centrality variations of 3%, 5%, and 5% at 6A, 8A, and 10.8A GeV, respectively. Antiproton spectra could not be extracted at 40A GeV because of lack of statistics. At 158A GeV the normalized total (see Fig. 8) and midrapidity yields increase with impact parameter. Such a behavior is expected in case absorption plays a significant role or, equivalently, the baryon-rich collision system approaches chemical equilibrium [23].

We chose to compare our findings to the transport model calculations from the HSD and UrQMD codes. Although both models reproduce rapidity density distributions in p + p collisions only with significant deviations, as shown in Fig. 10, HSD gives a good description of the nuclear collision data at both energies (see upper rows in Figs. 11 and 12) in the region covered by NA49 measurements with deviations only at large rapidities. The UrQMD model calculations also fit the experimental distributions fairly well, although with larger discrepancies, which are most pronounced at midrapidity and in central collisions.

## ACKNOWLEDGMENTS

This work was supported by the U.S. Department of Energy Grant No. DE-FG03-97ER41020/A000, the Bundesministerium für Bildung und Forschung, Germany (Grant No. 06F 137), the Virtual Institute VI-146 of Helmholtz Gemeinschaft, Germany, the Polish Ministry of Science and Higher Education (Grants No. 1 P03B 006 30, No. 1 P03B 127 30, No. 0297/B/H03/2007/33, No. N N202 078735, and No. N N202 204638), the Hungarian Scientific Research Foundation (Grants No. T032648, No. T032293, and No. T043514), the Hungarian National Science Foundation, OTKA (Grant No. F034707), the Bulgarian National Science Fund (Grant No. Ph-09/05), the Croatian Ministry of Science, Education and Sport (Project No. 098-0982887-2878), and Stichting FOM, the Netherlands.

- 
- [1] W. Busza and A. S. Goldhaber, *Phys. Lett. B* **139**, 235 (1984).
  - [2] B. B. Back *et al.* (E917 Collaboration), *Phys. Rev. Lett.* **86**, 1970 (2001).
  - [3] H. Appelshäuser *et al.* (NA49 Collaboration), *Phys. Rev. Lett.* **82**, 2471 (1999).
  - [4] I. G. Bearden *et al.* (BRAHMS Collaboration), *Phys. Rev. Lett.* **93**, 102301 (2004).
  - [5] I. C. Arsene *et al.* (BRAHMS Collaboration), *Phys. Lett. B* **677**, 267 (2009).
  - [6] C. Alt *et al.* (NA49 Collaboration), *Phys. Rev. C* **73**, 044910 (2006).
  - [7] B. B. Back *et al.* (PHOBOS Collaboration), *Phys. Rev. C* **75**, 024910 (2007).
  - [8] B. B. Back *et al.* (PHOBOS Collaboration), *Phys. Rev. C* **74**, 021901(R) (2006).
  - [9] B. B. Back *et al.* (PHOBOS Collaboration), *Phys. Rev. Lett.* **91**, 052303 (2003).
  - [10] I. C. Arsene *et al.* (BRAHMS Collaboration), *Phys. Rev. C* **72**, 014908 (2005).
  - [11] J. Adams *et al.* (STAR Collaboration), *Phys. Rev. C* **70**, 041901 (2004).
  - [12] B. I. Abelev *et al.* (STAR Collaboration), *Phys. Rev. C* **79**, 034909 (2009).
  - [13] M. Utvić, Dipl. thesis, University of Frankfurt, 2008 [[https://edms.cern.ch/file/1103430/1/diploma\\_milicia\\_utvic\\_.pdf.pdf](https://edms.cern.ch/file/1103430/1/diploma_milicia_utvic_.pdf.pdf)]
  - [14] C. Alt *et al.* (NA49 Collaboration), *Phys. Rev. C* **77**, 024903 (2008).
  - [15] C. Alt *et al.* (NA49 Collaboration), *Phys. Rev. C* **78**, 044907 (2008).
  - [16] C. Alt *et al.* (NA49 Collaboration), *Phys. Rev. C* **78**, 034918 (2008).

- [17] S. V. Afanasiev *et al.* (NA49 Collaboration), *Nucl. Instrum. Methods A* **430**, 210 (1999).
- [18] A. Laszlo, Ph.D. thesis, KFKI Research Institute for Particle and Nuclear Physics, Budapest, 2008; CERN EDMS Id 942284.
- [19] K. Werner, *Phys. Rep.* **232**, 87 (1993).
- [20] C. Alt *et al.* (NA49 Collaboration), *Phys. Rev. C* **77**, 034906 (2008); details can be obtained from [<https://edms.cern.ch/file/885329/1/vetocal2.pdf>]
- [21] M. van Leeuwen, Ph.D. thesis, NIKHEF, Amsterdam, 2003; CERN EDMS Id 816033.
- [22] M. Goossens, GEANT: Detector Description and Simulation Tool, long writeup W5013 [<http://cdsweb.cern.ch/record/1073159/>].
- [23] F. Becattini, J. Manninen, and M. Gazdzicki, *Phys. Rev. C* **73**, 044905 (2006).
- [24] T. Anticic *et al.* (NA49 Collaboration), *Phys. Rev. C* **80**, 034906 (2009).
- [25] T. Anticic *et al.* (NA49 Collaboration), *Eur. Phys. J. C* **65**, 9 (2010).
- [26] H. Weber, E. L. Bratkovskaya, and H. Stöcker, *Phys. Rev. C* **66**, 054903 (2002).
- [27] H. Petersen, M. Bleicher, S. A. Bass, and H. Stöcker, [arXiv:0805.0567](https://arxiv.org/abs/0805.0567).
- [28] K. Eskola, K. Kajantie, and J. Lindfors, *Nucl. Phys. B* **323**, 37 (1989). The corresponding code can be run online on the website [<http://www-linux.gsi.de/~misko/overlap/>].